AAS 15-363

SPIN STATE ESTIMATION OF TUMBLING SMALL BODIES

Corwin Olson*, Ryan P. Russell†, and Shyam Bhaskaran‡

It is expected that a non-trivial percentage of small bodies that future missions may visit are tumbling in non-principal axis rotation. An Extended Kalman Filter (EKF) Simultaneous Localization and Mapping (SLAM) method is used to estimate the small body spin state with optical landmark measurements, as well as the spacecraft position, velocity, attitude, and surface landmark locations. An example scenario based on the Rosetta mission is used, with a tumbling small body. The SLAM method proves effective, with order of magnitude decreases in the spacecraft and small body spin state errors after less than a quarter of the comet characterization phase. Initial small body angular velocity errors can be several times larger than the true rates, and the SLAM method will still converge (effectively having no apriori knowledge of the angular velocity). It is also observed that higher levels of tumbling in the small body increase the spin state angular velocity estimation errors and decrease the moments of inertia error, as expected.

INTRODUCTION

Determining the spin state of small bodies is one of the primary challenges spacecraft mission planners and navigators face during the early arrival mission stages at small bodies. As the Rosetta spacecraft approached Comet 67P/Churyumov–Gerasimenko in the summer of 2014, mission navigators at NASA's Jet Propulsion Laboratory doing shadow navigation[1] for ESA could not be certain that the comet was in principal axis rotation, despite some estimates provided by Hubble observation campaigns in 2003.[2] It is expected that a non-trivial number of small bodies in the solar system are "tumbling,",[3] i.e. in "complex rotation", and thus a tool was needed to provide an initial estimate of the spin state in case the comet was found to be tumbling upon arrival. Note that the term "tumbling' is used to indicate that the body is in non-principal axis rotation, and not that the motion is truly chaotic, as torque free motion is fully predictable using elliptic integrals.[4]

An Extended Kalman Filter (EKF) Simultaneous Localization and Mapping (SLAM) method is employed for this purpose. SLAM is traditionally associated with ground-based robotics, and most applications of SLAM in the literature use optical and range measurements to estimate the vehicle state and the environment around the vehicle.[5] The method proposed in this paper differs from traditional ground-based SLAM scenarios by estimating the spin state of a small body using standard optical landmark observations, and uses a spacecraft attitude estimate provided by a separate attitude determination using star trackers and gyros. The method described below also differs from previous applications of SLAM in the field of small body navigation[6] by estimating the spin state of the body simultaneously with the relevant inertial spacecraft states (instead of relative to a particular body-fixed frame on the surface of the body).

The estimation process occurs during the early small body characterization phase, when the spacecraft is many small body radii away from the body. A camera with a narrow field of view and long focal length is used, which makes significant numbers of landmarks visible. The optical navigation method using landmarks is well established in the literature.[7,8,9] The objective of this paper is to assess the ability of the EKF SLAM

*Graduate Student, Department of Aerospace Engineering and Engineering Mechanics, 1 University Station, University of Texas at Austin, Austin, Texas 78712-0235.

†Assistant Professor, Department of Aerospace Engineering and Engineering Mechanics, 1 University Station, C0600, University of Texas at Austin, Austin, Texas 78712-0235.

‡Supervisor, Outer Planet Navigation Group, Mission Design and Navigation Section, Jet Propulsion Laboratory, California Institute of Technology, MS 264-820, 4800 Oak Grove Dr., Pasadena, CA 91191.

algorithm to estimate the small body spin state (along with other state parameters), and determine the practical limits of how much initial small body spin state error the algorithm can handle.

The spin state of a small body can also be estimated independently with standard batch methods, solving for the pole direction, nutation, precession, and spin as described in the IAU models for planetary body attitude representation.[10] However, this representation is not feasible for tumbling small bodies, as the pole direction changes continually and thus there is no clear nutation, precession, and spin about the pole.

The estimated states include the inertial spacecraft position, velocity, and attitude; the small body spin orientation, angular velocity, mass, and moments of inertia; and the body-fixed landmark positions on the surface of the small body. These quantities are estimated directly from the pixel and line optical measurements of the surface landmarks, along with an initial spacecraft attitude estimate from an independent onboard attitude determination system consisting of gyroscopes, star cameras, and an attitude determination filter. The attitude provided is included in the estimation state and is further corrected using the optical landmark measurements. This further correction of the attitude is more important when the attitude estimates provided by the independent attitude determination system are degraded. Euler angles are used to represent the spacecraft attitude for ease of implementation, and Modified Rodrigues Parameters are used to represent the orientation of the small body in order to avoid singularities (through the standard shadow switching method).[11] Monte Carlo analyses are employed to statistically evaluate the filter's performance.

Note that the gravity spherical harmonic coefficients (beyond the GM) are assumed not known by the onboard models and are not estimated in this paper, as the altitudes of the spacecraft during this mission phase prevent significant observability of the coefficients (though estimation of the moments of inertia provides information for the degree 2 terms). It is shown below that only the GM is needed to successfully estimate the spin state.

On the other hand, a rough shape model of the small body for navigation purposes is assumed to be provided, and is necessary in the measurement models for the SLAM method to successfully estimate the spin state. The shape model is generated using ensemble photos from the approach phase, so it is reasonable to assume a reasonable approximation for the shape is available at the beginning of the small body characterization phase. In this paper, the complications of a realistic shape model are avoided by using a triaxial ellipsoid. However, the shape model for the truth and nominal measurement models can be set to a more complex model with minimal effect on the estimation results as long as the models are relatively consistent.

The shape model and gravity field are not further estimated in this paper. These are critical models for successful navigation in a small body mission, but the focus of this paper is on the estimation of the spin state, which must be performed in the small body characterization phase of a mission for successful navigation to lower orbits where the gravity field and shape model can be more accurately estimated.

Fortunately Comet 67P/Churyumov–Gerasimenko was found to be primarily in principal axis rotation, and thus the established tools were sufficient for the navigation task. However, it is estimated that a significant fraction of small bodies in the solar system are tumbling. Most tumbling bodies are smaller (less than 10 kilometers in diameter) and slow rotators (with rotational period greater than two days), but small fast rotators that are also tumbling have been detected as well.[12] In general it is not possible to know with strong certainty the degree to which a small body is tumbling before arriving at the body, especially for bodies that never closely approach the Earth. Thus, techniques to estimate the spin state for large deviations of the small body angular velocity are highly relevant for future missions to small bodies, especially those that are less than 10 kilometers in diameter.

OPTICAL NAVIGATION USING LANDMARKS

Many types of measurements can be used for autonomous navigation, including radar, lidar, and optical. The estimation algorithm proposed uses only optical measurements, which has strong advantages in terms of cost and ease of implementation. The camera used in the simulations is assumed to be comparable to the Charge-Coupled Device (CCD) cameras used for navigation in previous small body missions. Specifically, the simulated camera has a focal length of 140 mm and a sensor array of 1024 by 1024 pixels, for a total field-of-view (FOV) of approximately 5 degrees. The results of this paper are generally applicable to any CCD with a similar focal length, pixel array size, and FOV; which includes navigation cameras for the Rosetta (focal

length of 152 mm),[13] Dawn (focal length of 150 mm),[14] NEAR Shoemaker (focal length of 168 mm),[15] and Hayabusa (focal length of 120 mm).[16]

The optical measurements are the line-of-sight direction vectors from the spacecraft to the landmarks on the surface of the small body, whose initial body-fixed locations are assumed to be known to within the distance the user defines as the initial landmark position error. The term "body-fixed" refers to the frame fixed to and centered on the small body (not the spacecraft). Landmarks are defined as the central points of maps generated using the stereo-photoclinometry (SPC) method, which is a correlation technique that uses detailed topographic and albedo maps of the surface.[17] The process of using these landmark measurements to estimate the spacecraft position, velocity, and attitude are described in detail in previous studies,[7,8] but a brief overview of the fundamentals is given below. The same process is used to also estimate the small body spin state current orientation, angular velocity, mass, moments of inertia, and surface landmark locations.

It is assumed that an approximate value for the GM and a shape model have been previously determined in the first approach phase, and an initial set of landmarks has been identified on the surface. The SPC landmark identification problem is not treated here, but the positions of the landmarks contain some initial error that is estimated using the SLAM algorithm. A triaxial ellipsoid is used for the small body shape: while not as representative as a full polyhedron shape model, it is sufficient for the evaluation of the navigation algorithms. Night shading has been implemented in the current analysis, but the small body characterization trajectories stay primarily between the sun and the small body, so landmarks remain visible throughout the simulation. Camera distortion effects on the images that are typically calibrated in flight are not included in the simulations.

A simplified version of the landmarks observation computation is as follows. To start, the vector from the spacecraft to the j^{th} landmark is given by the equation

$$\boldsymbol{O_j} = \boldsymbol{L_j} - \boldsymbol{S} \tag{1}$$

where $\boldsymbol{L_j}$ is the body-fixed landmark position, and $\boldsymbol{S}$ is the Cartesian spacecraft position in the body-fixed frame. This vector can be transformed to inertial coordinates using the rotation matrix $\boldsymbol{R_{b2i}}$, which is computed using the current small body orientation parameters in the estimated state.

The camera is assumed to be hard-mounted to the spacecraft bus, with the camera boresight along the spacecraft z-axis for simplicity. Thus the camera frame is synonymous with the spacecraft-fixed frame, which is defined by the transformation

$$\boldsymbol{O_{c_j}} = \boldsymbol{R_{i2c}}\boldsymbol{R_{b2i}}\boldsymbol{O_j} \tag{2}$$

where $\boldsymbol{R_{i2c}}$ is defined by

$$\boldsymbol{R_{i2c}} = \boldsymbol{R_3}(\phi_{sc})\boldsymbol{R_2}(\frac{\pi}{2} - \delta_{sc})\boldsymbol{R_3}(\alpha_{sc}) \tag{3}$$

In equation 3, $\boldsymbol{R_3}(\phi_{sc})$ is a rotation about the Z-axis by the spacecraft twist angle ϕ_{sc}, $\boldsymbol{R_2}(\frac{\pi}{2} - \delta_{sc})$ is a rotation about the Y-axis by the declination value δ_{sc} subtracted from 90 degrees, and $\boldsymbol{R_3}(\alpha_{sc})$ is a rotation about the Z-axis by the right ascension (RA) angle α_{sc}. The declination is subtracted from 90 degrees to avoid singularities.

This LOS vector $\boldsymbol{O_{c_j}}$ in camera coordinates is then transformed into the two-dimensional camera focal plane using the gnomonic projection (which maps points on a sphere onto a plane)[18]

$$\begin{bmatrix} x_j \\ y_j \end{bmatrix} = \frac{f}{O_{c_j}[1]} \begin{bmatrix} O_{c_j}[2] \\ O_{c_j}[3] \end{bmatrix} \tag{4}$$

where f is the camera focal length (typically in millimeters). These focal plane coordinates x_j and y_j are transformed into pixel and line values, i.e. the horizontal and vertical pixel location within the picture, with the equation

$$\begin{bmatrix} p_j \\ l_j \end{bmatrix} = \begin{bmatrix} K_x & K_{xy} & K_{xxy} \\ K_{yx} & K_y & K_{yxy} \end{bmatrix} \begin{bmatrix} x_j \\ y_j \\ x_j y_j \end{bmatrix} + \begin{bmatrix} p_0 \\ l_0 \end{bmatrix} \tag{5}$$

where the elements of the **K** matrix are the vertical and horizontal pixel densities of the sensor array (typically in pixels per millimeters), and are calibrated using star fields in a mission. The center pixel and line values are p_0 and l_0, respectively. Note that that Eq. (5) produces values in increments smaller than individual pixels, as modern image processing capabilities can generate landmark center values at sub-pixel precision. In this simulation, the diagonal terms K_x and K_y are set to heritage values of 83.333[8] and the off-diagonal terms are set to zero. The above equations are used for both the truth and filter measurement models, and the measurement errors are described in the section titled "Monte Carlo Error Parameters".

Estimation Filter Architecture

A standard discrete EKF, as described by Tapley, et. al.,[19] is employed. The following parameters are estimated: the spacecraft position, velocity, and attitude; the small body spin state orientation, angular velocity, mass, and moments of inertia; and all of the surface landmark locations considered for navigation. Note that in this implementation, the size of the state vector is constant and does not change depending on how many landmarks are visible. These states are simultaneously estimated directly from 1) the landmark observations and 2) the attitude provided onboard independently from an attitude determination system consisting of star camera, gyros, and an attitude estimation filter. It is assumed that the spacecraft is commanded to point its camera at the center of mass of the small body using onboard position and attitude knowledge at every picture time using control moment gyroscopes (CMG), reaction wheels, or thrusters. Assuming that the attitude control error is low enough that a sufficient number of landmarks are in the camera FOV, the more important aspect for navigation analysis is the attitude knowledge error. The attitude knowledge error is simulated using expected attitude knowledge accuracy from modern onboard attitude determination systems.[20,21,22] It also assumed that stars are readily available to the star camera (i.e. the small body does not fill or nearly fill the star camera FOV). This assumption is reasonable during a small body characterization phase, as the FOV for the star camera is much wider than the narrow 5 degree FOV of the navigation camera.

By using the independently estimated attitude from an onboard attitude determination system, there is some "filter nesting". However, the measurements used for the independent attitude estimation (stars) are different than those used in the EKF SLAM filter (surface landmarks) to further refine the attitude estimate. Thus, there are no issues regarding "double counting" of measurements. And by using the estimated attitude from the onboard attitude determination system, there is no need to dynamically propagate the spacecraft attitude between picture times. This approach also obviates the need to directly compute and incorporate attitude maneuvers, which significantly simplifies the simulation and is based on previous published work.[7,11]

Of course any estimate will have some error associated with it, and historical performance from previous missions can inform the analyst on what the typical level of error is for onboard attitude determination systems. High accuracy attitude determination system estimates are likely to be available on any future missions to small bodies, and thus the errors associated with these estimates are representative of what can be expected in future missions to small bodies.

Impulsive maneuvers are performed in the simulation to allow the full small body characterization phase to be included in the estimation process. Typically the maneuver is planned using the most recent best estimate of the spacecraft state, propagated forward to the maneuver time. This maneuver is performed, and some execution error occurs. Thus, the truth maneuver can be thought of as the summation of the nominal planned maneuver and the execution error. However, in this estimation analysis, it is not the execution error that matters, but rather the knowledge error of the maneuver (assuming the execution error is not so large such that the nature and availability of the observations change). In other words, the difference between the planned maneuver and the performed maneuver (the execution error) is far less important for navigation analysis than the difference between the true performed maneuver and the best estimate of the performed maneuver. Thus, execution error can be "chosen" by the analyst such that for every maneuver, the execution error plus the planned maneuver is equal to a precomputed truth delta-v. This method has the strong advantage of allowing a single constant truth trajectory for all Monte Carlo trials, and has been used in navigation analysis for NASA's Magnetosphere Multiscale (MMS) mission.[23]

During the performance of the maneuver, onboard sensors such as accelerometers, gyroscopes, and thruster sensors collect measurements and a separate maneuver estimation process is performed using these independent measurements (like the separate attitude estimation process using independent star and gyro measure-

ments). The output estimate of the maneuver can be considered a summation of the true maneuver and the estimate knowledge error.

To emulate the process of estimating the maneuver, a conservative amount of knowledge error is sampled using user-provided error sigmas and added to the constant impulsive truth maneuver. This delta-v sum is added to the nominal state at the maneuver time, and the velocity portion of the state covariance is inflated using the approximate 1-sigma values of the knowledge error. For this analysis, typical conservative maneuver execution error parameters are used for the knowledge error parameters, which adds another layer of conservatism: usually the post-fit knowledge error of a maneuver is far less than the maneuver performance execution error. The diagram in Figure 1 illustrates this method of introducing maneuver knowledge error. The magnitudes of the differences in the velocities are exaggerated for illustrative purposes.

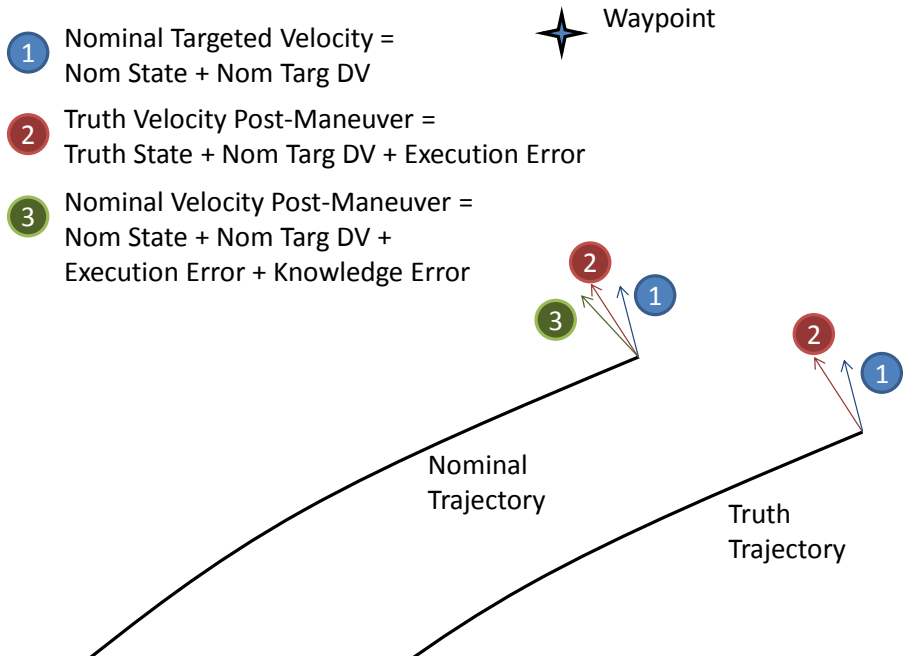

Figure 1: Maneuver Diagram

The precomputed truth maneuvers are generated for each truth scenario considered, using a standard differential correction method to target the trajectory way-points. These maneuvers are saved and then provided as inputs for the Monte Carlo analysis, as they are constant for all trials. If the truth scenario is modified, these delta-v values must be recomputed, though it is observed that the delta-v values have low sensitivity to changes in the truth small body spin state.

Dynamical Models

The truth spacecraft dynamical trajectory model includes central body acceleration, perturbations from a spherical harmonic gravity field, solar radiation pressure (SRP), and the third body perturbation (TBP) of the Sun. Accelerations from other bodies are negligible and not included. The nominal spacecraft dynamical trajectory model includes the same accelerations except for the spherical harmonic gravity perturbations, which are completely neglected: at this point in a small body mission, no reliable gravity harmonic coefficient values are available. Some estimates of the lower order coefficients with likely significant errors may be available from shape models and assumed constant density profiles,[24,25] but these are unnecessary for navigation at the high altitude characterization phase. The gravity field can be further refined once a spin state is established and lower orbits are achieved.

A fourth degree and order spherical harmonic gravity model from the asteroid Eros is used for the truth model, though the GM and reference radius are altered to the current best estimate of Comet 67P/Churyumov–

Gerasimenko. The spherical harmonic coefficients for Comet 67P/Churyumov–Gerasimenko are not yet available to the public (to the authors' knowledge), so the coefficients of Eros are used to emulate the level of perturbations expected at a small body. The coefficients used are an approximation of a higher order field that would be used in actual mission. See Table 1 for the relative magnitudes of the forces acting on the spacecraft when it is furthest and closest to the small body during the simulation.

Table 1: Forces On Spacecraft [N]

	Maximum Radius (115 km)	**Minimum Radius (54 km)**
Central Body	7.176×10^{-5}	3.255×10^{-4}
Gravity Pert	1.022×10^{-8}	2.424×10^{-7}
SRP	2.325×10^{-6}	2.325×10^{-6}
TBP	2.186×10^{-7}	1.151×10^{-7}

When the spacecraft is at the maximum position radius of approximately 115 kilometers, which occurs at the start time of the simulation, the gravity perturbation is weaker than the SRP and TBP forces. When the spacecraft has a minimum radius of approximately 54 km, which occurs halfway through the final trajectory arc of the simulation, the gravity perturbation is twice as strong as the TBP force, but still an order of magnitude weaker than the SRP. Thus, throughout the simulation, the SRP is the most important perturbation force to consider for the spacecraft dynamics. Neglecting the gravity perturbation at these high altitudes in the nominal dynamics model has minimal effect on the estimates.

The small body rotation dynamical model is a simple integration of Euler's equations. No torques from YORP effects, out-gassing effects, other celestial bodies are included in the dynamics, as these are expected to be negligible over the time span of the simulation.[4] The small body angular velocity is expressed within the simulation in the body-fixed frame so that the moments of inertia are constant over the integration time spans (though they are updated at the measurement updates).

Note that the spacecraft and small body dynamics are propagated via numerical integration between picture times using variable step RK7(8) propagation, with relative and absolute error tolerances set to 10^{-15}. A low tolerance is required for the faster tumbling scenarios when the small body orientation values are rapidly changing. The covariance is propagated to the same times, also using variable step propagation, by the standard method of integrating the state transition matrix via numerical integration.

SIMULATION SCENARIO

The scenario used to evaluate the SLAM algorithm is based on the comet characterization phase of the Rosetta mission,[26,20] when the spacecraft starts at approximately 115 kilometers from the body, and flies in pyramid-like trajectories between the comet and the sun.[27] Only a small amount of delta-v is needed to shift between hyperbolic trajectories at high altitudes above a small body, allowing improved viewing geometries for the small body characterization phase.

Eight arcs of the pyramid trajectory are simulated, which are displayed in the three dimensional plot and the set of two dimensional projections in Figure 2. Note that the arrow in Figure 2a is the direction towards the Sun, and the Brillouin sphere of the body is shown. The arcs are shown in a Sun-Fixed frame only for easier comprehension, with the dynamics integrated in the inertial frame.

The orbital elements for all eight arcs are provided in Figure 3. Note that only the mean anomaly changes significantly between maneuver times, and that the semi-major axis is negative, both a result of hyperbolic nature of the trajectories.[2] Thus, the arcs are plotted separately to allow the reader to see the smaller variations in the elements between maneuvers.

To represent the orientation of the small body, Modified Rodrigues Parameters (MRP) are used.[28] The initial Euler angle values provided are converted to MRP at the start of the simulation, and the output MRP truth and error values are converted to Euler angles for a more intuitive representation. The MRP representation has a number of advantages over Euler angles and quaternions. First, the method described in Karlgaard[11]

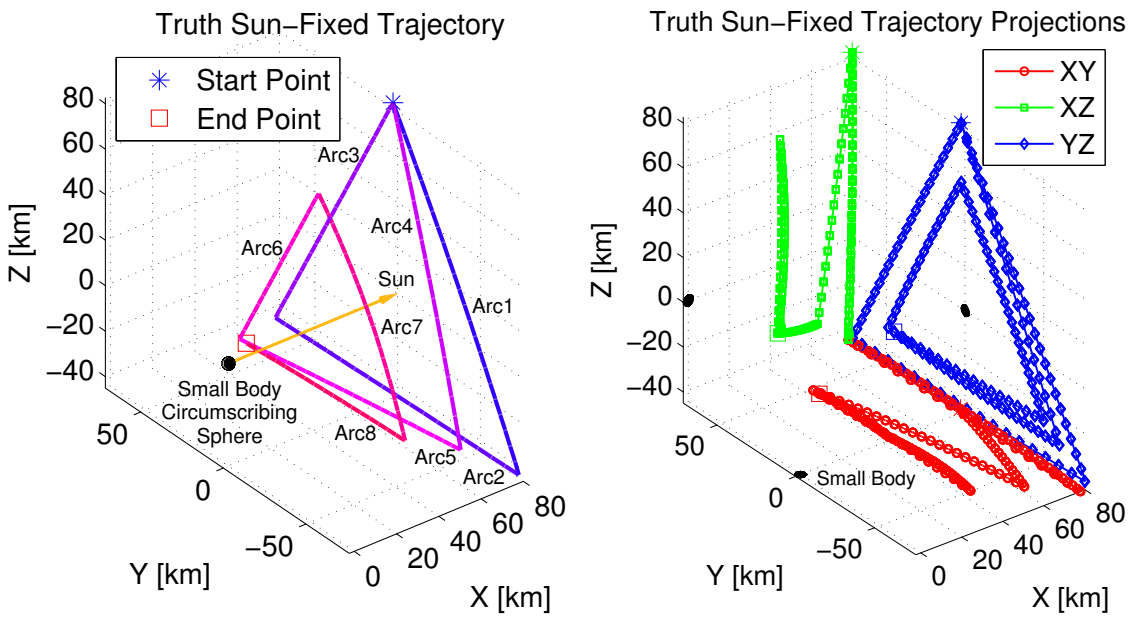

(a) Truth Sun-Fixed Trajectory

(b) Trajectory Projections of Sun-Fixed Trajectory

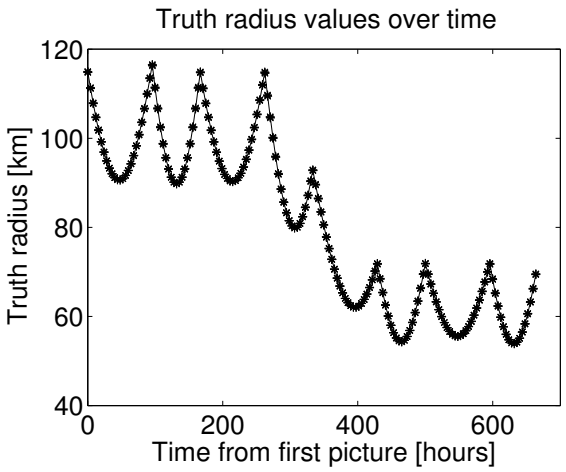

(c) Truth Radius

Figure 2: Truth Trajectory

shows how singularities can be avoided by switching to shadow MRP values when the magnitude of the MRP vector exceeds one, which is equivalent to a rotation of 180 degrees (and thus exactly halfway between the singularities of the standard MRP set and the shadow MRP set). The dynamical propagation and filter update equations are identical for the standard MRP and shadow MRP values, allowing a simple switch of the MRP to the shadow set (or vice versa) without concern for how it will impact the propagation or estimation of the attitude.

Second, Crassidis and Markley[28] show that the standard additive EKF is equivalent to the Multiplicative EKF for the MRP representation, which allows the small body attitude to be estimated simultaneously with the other states in the standard EKF. Third, it is shown in Karlgaard[11] that attitude estimation using the MRP with this switching method is computationally more efficient than other standard techniques such as the quaternion multiplicative EKF.

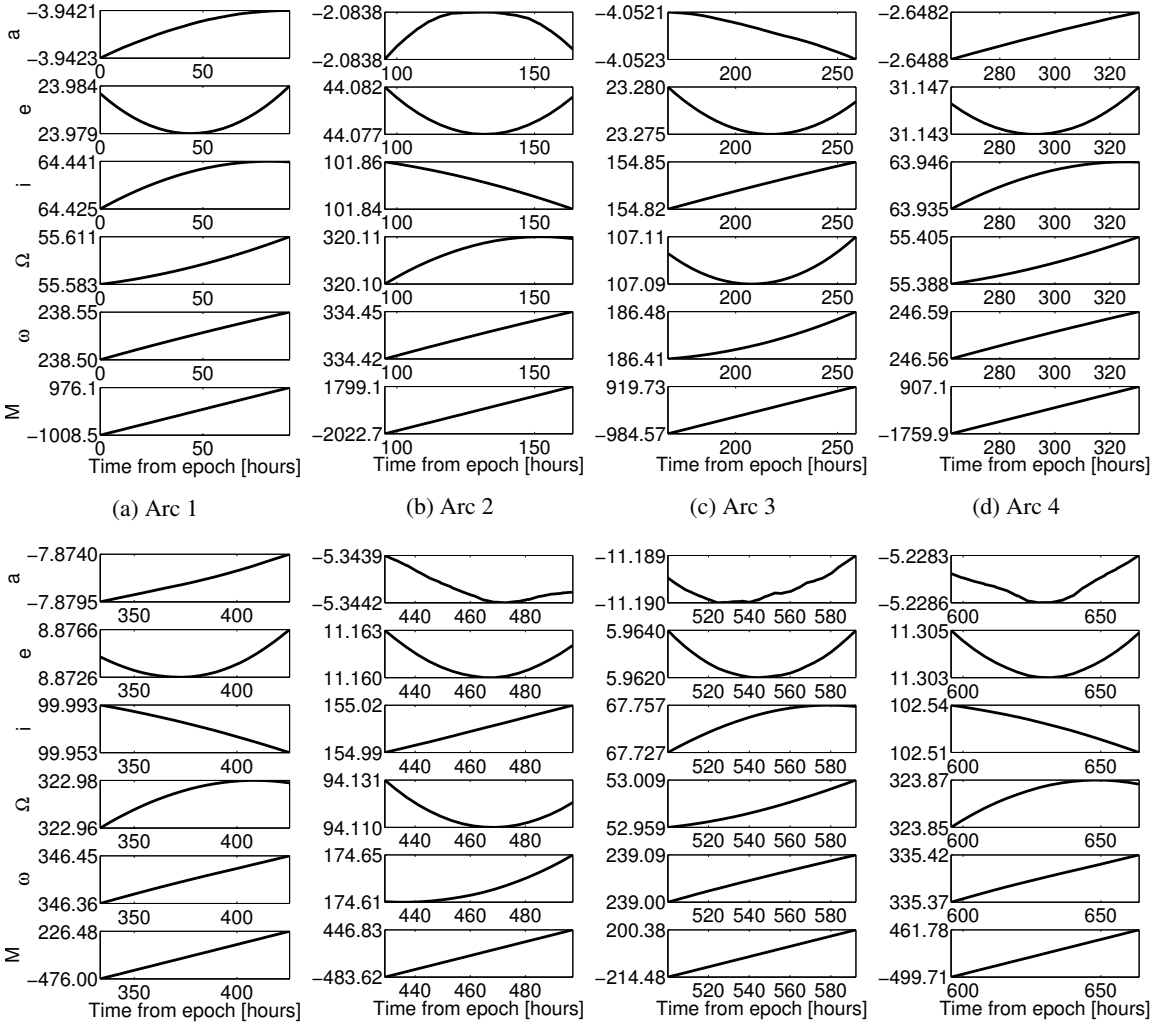

(a) Arc 1 (b) Arc 2 (c) Arc 3 (d) Arc 4

(e) Arc 5 (f) Arc 6 (g) Arc 7 (h) Arc 8

Figure 3: Truth Orbital Elements [km and deg]

Unlike the true Comet 67P/Churyumov–Gerasimenko, the small body in this scenario is made to tumble, with an angular velocity not closely aligned with the maximum principal axis of the body. Thus it is critical to use a non-singular attitude representation method, as a tumbling body can find it's way to any singularities that might exist in a standard three dimensional attitude representation. The truth small body spin state Euler angles and body-fixed angular velocity components for the nominal tumbling scenario are displayed in Figure 4. Note how the Right Ascension (RA) grows substantially with time, the declination (Dec) varies periodically from 0 to -180 degrees, and the Prime Meridian (PM) varies periodically as well. The angular velocity components also vary significantly.

Thirty predetermined and randomly located SPC landmarks are available for navigation, which are presumed to be a result of previous mapping in the initial approach phase. This number of landmarks is conservative relative to the range of sixty to one hundred landmarks that are expected for this stage of a small body mission.[1] However, including more than thirty landmarks in the simulation does not significantly enhance the estimation of the small body spin state in this scenario, and computation increases significantly with increasing state size. The association problem of the SPC landmarks in the SLAM method is not treated in this work.[29]

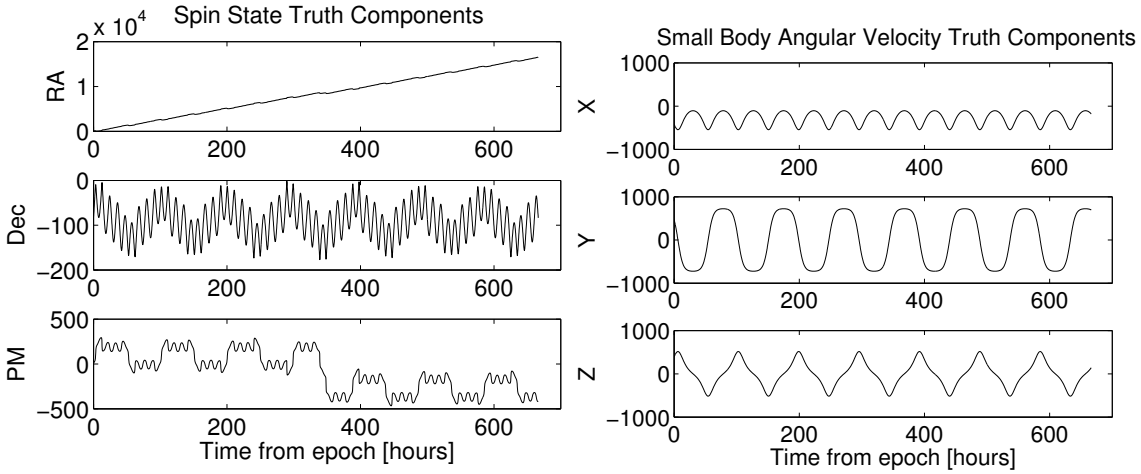

(a) Orientation [deg],
$\boldsymbol{R_{i2b}} = \boldsymbol{R_3}(\text{PM})\boldsymbol{R_1}(\frac{\pi}{2} - \text{Dec})\boldsymbol{R_3}(\text{RA})$

(b) Angular Velocity [deg/day]

Figure 4: Nominal Tumbling Small Body Spin State Over Time

All code is written in Fortran, using the latest 1995 and 2003 standards, and compiled using standard release mode settings in 2011 Intel Visual Fortran. All simulations are run on a single processor of a quad-core Intel Xeon CPU running at 3.60 GHz.

Various timing parameters of the simulation are listed in Table 2, including the maneuver times. The maneuvers, which range in magnitude from 0.87 m/s to 0.58 m/s, are displayed in Table 3 below. Maneuver knowledge error is added to these truth maneuvers, as explained in the "Estimation Filter Architecture" section above. The 1-sigma magnitude of the knowledge error is provided in Table 7 of the "Monte Carlo Error Parameters" section below. See Tables 4 and 5 for the parameters concerning the small body and the spacecraft, respectively. Note that the initial orientation and spin rates of the small body are provided in terms of Euler angles and Euler angle rates, which are converted to Modified Rodrigues Parameters and body-fixed angular velocity values in the initialization of the simulation.

Table 2: Simulation Timing

Simulation Parameter	Values
Epoch Time	06-Aug-2014 12:00:00.00
End Time	03-Sep-2014 06:40:00.00
Maneuver #1	10-Aug-2014 11:33:20.00
Maneuver #2	13-Aug-2014 10:40:00.00
Maneuver #3	17-Aug-2014 10:13:20.00
Maneuver #4	20-Aug-2014 09:20:00.00
Maneuver #5	24-Aug-2014 08:53:20.00
Maneuver #6	27-Aug-2014 08:00:00.00
Maneuver #7	31-Aug-2014 07:33:20.00
Minimum Time Before First Update	1 minute after epoch
Measurement Timing	4 photos 5 minutes apart, every 4 hours

Filter Parameters

The filter parameters used in the EKF are listed in Table 6. Note that the measurement noise covariance sigmas are slightly higher than one might expect given the measurement error of 0.5 pixel (1-sigma), but this

Table 3: Simulation Maneuvers

Maneuver Count	Delta-V Vector [km/s]
#1	[-1.5511$\times10^{-4}$, -4.9783$\times10^{-4}$, 6.9638$\times10^{-4}$]
#2	[-4.8853$\times10^{-4}$, 1.6001$\times10^{-4}$, -6.9008$\times10^{-4}$]
#3	[7.1944$\times10^{-4}$, 3.8504$\times10^{-4}$, -1.63590$\times10^{-5}$]
#4	[-2.9441$\times10^{-4}$, -4.4434$\times10^{-4}$, 4.7151$\times10^{-4}$]
#5	[-3.4777$\times10^{-4}$, -2.7907$\times10^{-6}$, -4.6962$\times10^{-4}$]
#6	[5.2675$\times10^{-4}$, 1.7877$\times10^{-4}$, 4.8241$\times10^{-6}$]
#7	[-8.6991$\times10^{-5}$, -3.4001$\times10^{-4}$, 4.3964$\times10^{-4}$]

Table 4: Small Body Properties

Simulation Parameter	Truth Values
Initial Pole Right Ascension	3 deg
Initial Pole Right Ascension Rate	450 deg/day
Initial Pole Declination	4 deg
Initial Pole Declination Rate	450 deg/day
Longitude of the Prime Meridian at Epoch	5 deg
Rotation Rate	350 deg/day
GM	6.67384x10^{-7} km^3/s^2
Reference Radius for Gravitational Harmonics	2.375 km
Max Radius	2.375 km
Intermediate Radius	1.885 km
Min Radius	1.470 km
Max Moment of Inertia	2.22289x10^{13} km^2-kg
Intermediate Moment of Inertia	1.88625x10^{13} km^2-kg
Min Moment of Inertia	1.38156x10^{13} km^2-kg
Number of Landmarks on surface	30
Degree and Order of Gravity Harmonics	4 (Eros Values Used)

Table 5: Spacecraft Properties

Simulation Parameter	Truth Values
Mass	1422 kg
Area	6 m^2
Reflectivity Coefficient	1.1
Initial Position (Inertial)	[-47.417, -98.777, -34.924] km
Initial Velocity (Inertial)	[2.8411x10^{-4}, 2.3799x10^{-4}, -2.0866x10^{-4}] km/s

measurement underweighting produces consistently slightly better results. It has been shown in the literature that measurement underweighting often produces the lowest navigation errors.[30,31]

To prevent the position uncertainty from locking down too quickly, which can cause issues with the estimation of other parameters such as the spacecraft attitude, a small amount of additional process noise (100 square meters) is added to the prefit position uncertainty at the second picture time. This "damping" of the covariance reduction allows a smooth transition from the larger initial corrections of the state estimates to the steady state behavior.

The uncertainty added to the spacecraft velocity at maneuver times, as described in the "Estimation Filter Architecture" section above, is provided in units of $(km/s)^2$. These values are added directly to the spacecraft velocity diagonal values of the state covariance matrix after it is mapped from the previous estimation time to the maneuver time.

Note that the units of the process noise for attitude are degrees squared, and not degrees squared per time cubed, as this process noise is applied directly to the attitude uncertainty, rather than integrated over time like the process noise for position and velocity. This direct application of the process noise is logical because the attitude is not dynamically propagated, as explained previously. Similarly, the process noise for the spin state angles and angular velocity are values added directly to the mapped covariance diagonal terms.

Table 6: Filter Parameters

Simulation Parameter	Values
Initial Filter Position Covariance (1-σ)	[1, 1, 10] km
Initial Filter Velocity Covariance (1-σ)	[$1x10^{-5}$, $1x10^{-5}$, $1x10^{-5}$] km/s
Initial Filter Attitude Covariance (1-σ)	[0.02, 0.02, 0.02] deg
Initial Filter Small Body Spin State Angles Covariance (1-σ)	[5, 5, 5] deg
Initial Filter Small Body Spin State Angular Velocity Covariance (1-σ)	[10, 10, 10] deg/day
Initial Filter Small Body GM Covariance (1-σ)	$1.4x10^{-7}$ km^3/s^2
Initial Filter Small Body Moments of Inertia Covariance (1-σ)	[$3x10^{11}$, $3x10^{11}$, $3x10^{11}$] km^2-kg
Initial Filter Small Body Landmark Position Covariance (1-σ)	[0.01, 0.01, 0.01] km
Measurement Noise Covariance (1-σ)	[1, 1] pixels
Process Noise q for Position and Velocity	$1x10^{-16}$ km^2/s^3
Process Noise for Attitude	$4x10^{-7}$ deg^2
Process Noise for Spin State Orientation (MRP)	$1x10^{-6}$
Process Noise for Spin State Angular Velocity	$1x10^{-12}$ $(deg/day)^2$
Velocity Covariance Inflation For Maneuvers	$4x10^{-10}$ $(km/s)^2$

Monte Carlo Error Parameters

If the process and measurements models are exact and linear, and the noise in the data is truly random and Gaussian, then the covariance obtained from the filter completely and accurately represents the uncertainty of the estimate. Of course, the dynamics and measurements are nonlinear and the other conditions are never fully met in a real mission, nor in the current simulation. Thus Monte Carlo simulations are used to obtain a realistic assessment of the filter accuracy. The 1-σ simulation error parameters sampled in the Monte Carlo simulations are listed in Table 7, where the errors for the position and velocity are provided in the View 2 frame: the first axis is along the velocity vector, the second axis is perpendicular to the orbital plane, and the third axis is perpendicular to the first and second, in general pointing zenith. This frame is chosen for the errors based on how missions have historically broken down the expected navigation performance errors. The initial filter covariance values for the position and velocity are given in the same reference frame.

The initial small body orientation and spin rates errors are provided by the user in terms of Euler angles and Euler angle rates, like initial truth values. These values are converted to Modified Rodrigues Parameters errors and body-fixed angular velocity errors in the initialization of the simulation using first order partial derivative matrices. The same conversion process is performed for the initial filter covariance values.

Note that modern image processing capabilities can generate landmark center values at sub-pixel precision, and thus 0.5 pixel errors are used in this simulation. Also note that the initial state errors are lower than those associated with ground tracking estimation, as the expected state errors from optical navigation in the

Table 7: 1-σ Monte Carlo Error Parameters

Simulation Parameter	1-σ Error Values
Spacecraft Mass	20 kg
Spacecraft Area	1 m^2
Spacecraft Initial Position	[1, 1, 10] km
Spacecraft Initial Velocity	[1x10^{-5},1x10^{-5},1x10^{-5}] km/s
Spacecraft Attitude	[0.02, 0.02, 0.02] deg
Small Body Initial Attitude	[5, 5, 5] deg
Small Body Initial Angular Velocity	[10, 10, 10] deg/day
Small Body Initial GM	1.4x10^{-7} km^3/s^2
Small Body Initial Moment of Inertia	[3x10^{11}, 3x10^{11}, 3x10^{11}] km^2-kg
Small Body Initial Landmark Locations	[0.01, 0.01, 0.01] km
Observation	[0.5, 0.5] pixel
Maneuver Magnitude	1%
Maneuver Direction	1 deg Right Ascension, 1 deg Declination

approach phase (which occurs immediately prior to the small body characterization phase) are used instead. The process noise values in Table 6 are selected such that the covariance reasonably well represents the error distribution of the Monte Carlo simulation.

There are two primary methods to distribute initial state errors for a Monte Carlo analysis: starting with a nominal state and adding the initial state errors to obtain numerous different truth trajectories, or starting with a truth state and adding the initial state errors to obtain different initial nominal states. The advantage of the first method is that it emulates what occurs in flight operations: the truth state is never known, so Monte Carlo trials must be distributed about the downlinked best estimate of the state. The advantage of the second method is that there are not numerous different truth trajectories and observations, which can complicate comparison studies and force analysts to introduce initial state error with a more complex model than a standard Gaussian distribution to avoid situations like the truth intersecting with the small body. Because the intent of this paper is to assess the ability of the EKF SLAM algorithm to estimate the small body spin state, and determine the practical limits of how much the small body can tumble before the estimation algorithm breaks down, the latter option is chosen: the nominal states are distributed about the truth. A user set flag can be switched to the first option should the tool be needed for flight operations analysis. Similarly, the nominal attitude at each picture time is computed by "adding" (in the rotational sense) the computed attitude error to the truth pointing vector, which can also be reversed with a user set flag. As a result, all observations for the Monte Carlo trials are identical. And as stated before, all truth maneuvers are identical for all trials (with the execution error chosen such that no additional targeting for each nominal trajectory is necessary), and the nominal delta-v computed as a summation of the truth delta-v and the sampled maneuver knowledge errors.

The 1-sigma maneuver knowledge error parameters are defined in terms of magnitude and direction. The magnitude 1-sigma error value is 1% of the truth maneuver magnitude, added to the truth maneuver magnitude. No fixed magnitude error is assumed. The direction error values are provided in terms of spherical coordinates α_{mnvr} and δ_{mnvr}, where α_{mnvr} is the "Right Ascension" rotation about the true thrust vector and δ_{mnvr} is the "Declination" rotation away from that truth thrust vector. Both angles are 1 degree (1-sigma), and are not dependent on the maneuver magnitude. No magnitude dependent component of the direction error is assumed. These knowledge error values are considered strongly conservative even for execution error, which is likely to be far greater than knowledge error, as explained in the "Estimation Filter Architecture" section above. A less conservative model would involve using knowledge errors previously determined for the mission, and would likely use a more complete Gates maneuver error model, which involves direct and proportional terms for both the magnitude and direction errors.[32]

RESULTS

A Monte Carlo analysis using one thousand trials is employed to verify the performance of the SLAM estimation algorithm for several different truth tumbling scenarios, two of which include a significant amount of tumbling in the small body. The number of Monte Carlo trials was increased until the ensemble error statistics converged for each of the scenarios, which are shown for the nominal tumbling scenario in the captions of the figures below. The nominal tumbling truth scenario is shown in Figure 4 above. The simulation takes approximately 70 minutes, with an average of approximately 4.2 seconds per trial.

Figure 5 shows the post-fit position and velocity ensemble error magnitude and covariance for the nominal tumbling Monte Carlo simulation. The initial error in both states are rapidly reduced to near steady state levels within two or three picture times, with order of magnitude reductions in the state error within one or two arcs of the comet characterization trajectory. The error introduced to the velocity at each maneuver time is quickly reduced by more than an order of magnitude after the maneuver, and the added error does not significantly disrupt the estimation of the other states.

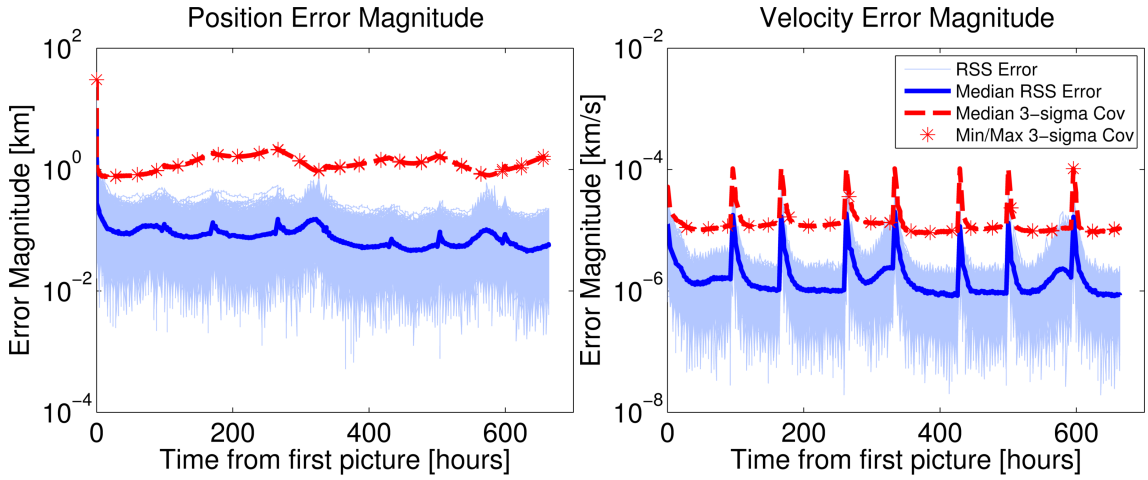

(a) Position
RMS: 0.4080, Max: 28.6948,
Steady State: 0.0587 km

(b) Velocity
RMS: 4.5979E-6, Max: 8.9609E-5,
Steady State: 8.6810E-7 km/s

Figure 5: Spacecraft Position and Velocity Error

Figure 6 shows the post-fit small body orientation and angular velocity ensemble error magnitude and covariance. These quantities also rapidly converge within several photographs of the surface. These results reveal that the spin state can be estimated with sufficient accuracy for spacecraft navigation in later mission phases as the spacecraft approaches the surface. Like the position and velocity errors, order of magnitude reductions in the state error are observed within a single arc of the eight hyperbolic arc trajectory. Note that the orientation errors and covariance are converted from MRP to Euler angles, and thus there are spikes in the covariance and (to a smaller extent) the error that do not appear in the MRP values. This discrepancy is due to the nature of the conversion from MRP to Euler angles, where certain MRP orientations produce partial derivative values of the Euler angles with respect to MRP that inflate the state uncertainty and error.

Figure 7 shows the post-fit small body gravitational parameter and moment of inertia ensemble error magnitude and covariance. The GM takes longer to converge than the spacecraft position and velocity, and the small body spin states, but the GM does prove observable. The moment of inertia error plot has a small initial reduction in the first arc, but does not show significant error reduction subsequently, indicating very limited observability of the moments of inertia.

Figure 8 shows the number of visible landmarks at each photo time (which is identical for all trials), as well as the post-fit position error magnitude and covariance for all of the landmarks for a single trial of the Monte Carlo analysis. The landmark body-fixed position errors are representative of the performance observed in

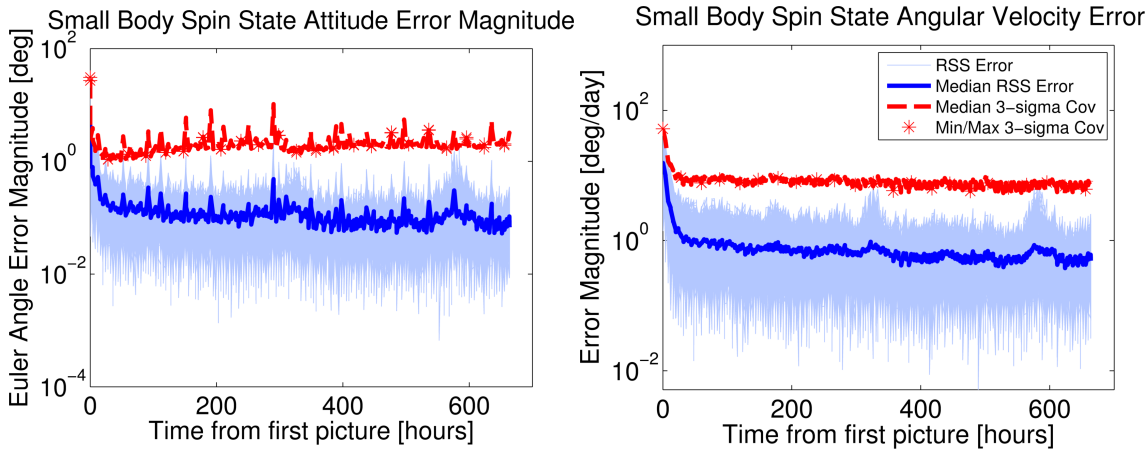

(a) Spin State Attitude
RMS: 0.3902, Max: 22.5270,
Steady State: 0.1055 deg

(b) Spin State Angular Velocity
RMS: 1.9532, Max: 42.2692,
Steady State: 0.4894 deg/day

Figure 6: Small Body Spin State Errors

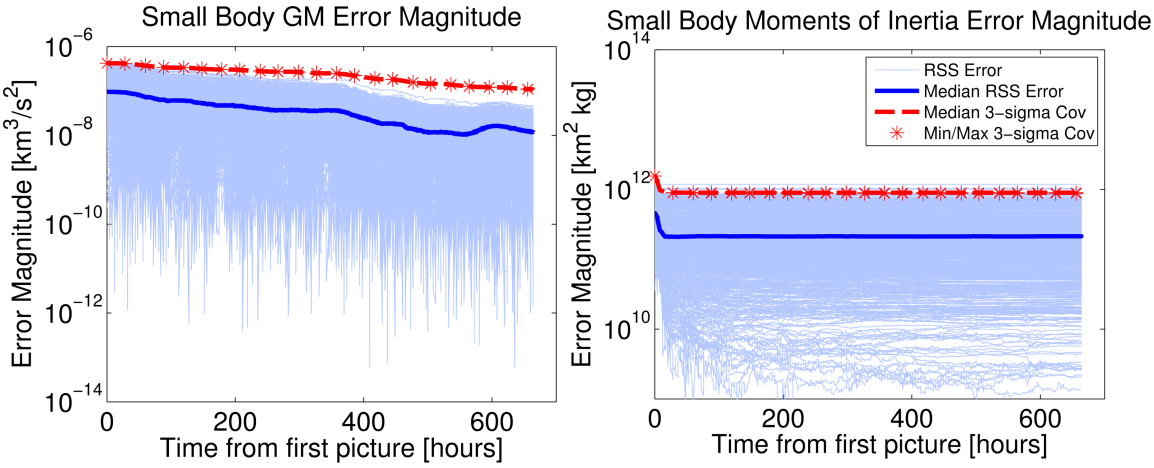

(a) Small Body GM
RMS: 6.3908E-8, Max: 4.4690E-7 km^3/s^2

(b) Small Body Moments of Inertia
RMS: 3.1022E+11, Max: 1.2251E+12 km^2-kg

Figure 7: Small Body Mass and Moment of Inertia Errors

the other trials. The landmark position error magnitude drops by a factor of at least three, with some error magnitudes dropping by a full order of magnitude.

Overall, the results for this nominal scenario show excellent convergence for all estimated states except for the moments of inertia (which are not significantly observable). Most importantly for this analysis, the small body spin state values quickly converge to the truth values, which correspond to a specific tumbling body scenario. The covariance values conservatively represent the uncertainty in the state, as the error plots are almost entirely contained within the 3-sigma covariance magnitudes. The postfit residuals are scattered evenly about zero, indicating no systematic biases, with an RMS of approximately 0.78 pixels. This RMS agrees with the Rosetta navigation results presented by Bhaskaran.[1]

It is observed that with higher spacecraft attitude errors introduced (corresponding to a degraded attitude determination system consisting of star cameras and gyros), the spin state angle errors grow significantly

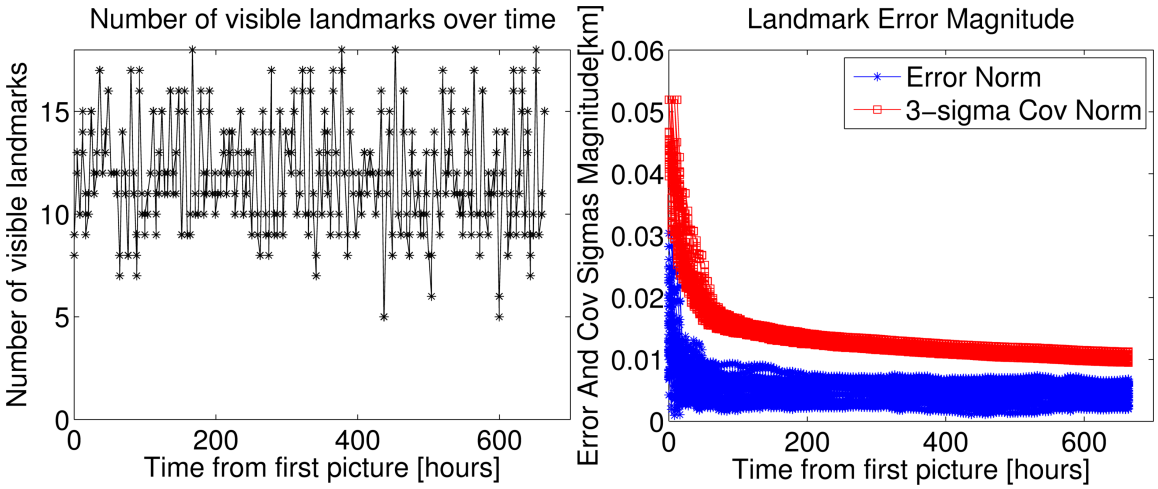

(a) Number of Visible Landmarks, All Trials

(b) Landmark Position Errors, Single Trial

Figure 8: Landmarks

larger and more volatile. The other state vectors also show greater instability, with some trials at least partially diverging in spacecraft position, velocity, and GM error. Larger initial position errors can also disrupt some of the trials, though the sensitivity is lower than for the attitude errors.

Using 1 pixel (1-sigma) for the measurement noise covariance produces slightly better results than using the 0.5 pixels (1-sigma) value that corresponds to the 0.5 pixels observation error. This measurement under-weighting, as described earlier, provides slightly better results but is not critical for successful convergence of the state parameters.

Starting with the error values listed in Table 7, the initial small body orientation and angular velocity errors (along with the associated initial uncertainties, which were matched to the error sigma values) are increased until the estimation process becomes intractable with the current filter process values. For this nominal scenario, the maximum initial small body attitude error magnitude is approximately 50 degrees (1-sigma). Beyond that value, the tuning parameters become insufficient to prevent large numbers of trials from greatly exceeding the covariance, and in some cases fully diverging. The maximum initial small body angular velocity error magnitude is approximately 1500 degrees per day (1-sigma), far larger than the initial angular velocity values of the body. This is fortunate, as the initial values for angular velocity of the body can be completely incorrect and the EKF-SLAM filter will still converge on the correct angular velocity, even for a highly tumbling body. Thus, the overall effectiveness of the filter is significantly less sensitive to increases in the initial small body angular velocity error than increases in the small body attitude error.

These limits are also assessed for two other truth spin state scenarios: a faster tumbling scenario with initial Euler angle spin rates of 900 deg/day for right ascension, 900 deg/day for declination, and 696 deg/day for prime meridian; and a non-tumbling scenario with initial Euler angle spin rates of 0 deg/day for right ascension, 0 deg/day for declination, and 696 deg/day for the prime meridian. The faster tumbling scenario has the same approximate limit on the initial angular velocity error as the nominal scenario (1500 deg/day), but a much lower limit on the initial orientation error (10 deg). This is not surprising, as higher tumbling rates will grow any initial orientation error much faster. The non-tumbling scenario has the same initial orientation error as the nominal scenario (50 degrees), but a higher limit on the initial angular velocity error (2000 deg/day) than the nominal. Of course the maximum initial spin state errors are likely to be different for other levels of truth tumbling, but these values give the reader a sense of the approximate accuracies needed for initial spin state estimation in different types of scenarios.

The statistical performances of the SLAM algorithm in the three different truth tumbling scenarios are compared, with identical initial spin state errors for all three scenarios. One thousand Monte Carlo Trials are

generated for each scenario, and the results are shown in Table 8 below. All simulations take approximately 70 to 75 minutes.

Table 8: Ensemble RMS Errors For Different Tumbling Scenarios

	Faster Tumbling (900, 900, 696)* deg/day	**Nominal Tumbling (450, 450, 350)* deg/day**	**No Tumbling (0, 0, 696)* deg/day**
Position [km]	0.4076	0.4080	0.4077
Velocity [km/s]	4.5514×10^{-6}	4.5675×10^{-6}	5.1233×10^{-6}
Spin State Orientation (MRP)	0.0022	0.0022	0.0022
Spin State Angular Velocity [deg/day]	2.8272	1.9532	1.7129
Small Body GM [km^3/s^2]	6.3778×10^{-8}	6.3908×10^{-8}	6.4337×10^{-8}
Moments of Inertia [km^2-kg]	3.1279×10^{11}	3.1022×10^{11}	5.3781×10^{11}

* The initial Euler angle rates (RA rate, Dec rate, PM rate), converted to angular velocity

The ensemble spin state orientation MRP RMS errors are equal to four digits in the three scenarios, suggesting that orientation error is not strongly dependent on the level of tumbling. The ensemble spin state angular velocity RMS error is 12.3% lower in the non-tumbling case and 44.8% higher in the faster tumbling case. Thus, the level of tumbling does strongly affect how accurately the spin state angular velocity is estimated.

The RMS position errors are not significantly different among the three scenarios. The RMS velocity errors for the faster and nominal tumbling approximately equal, but the non-tumbling scenario does have slightly higher velocity error (12.2%). The small body GM error is not significantly different among the three scenarios. The moments of inertia error is approximately the same in the faster tumbling and nominal tumbling scenarios, but 73.4% higher in the non-tumbling case. The significant increase in the moments of inertia error is not surprising, as the lack of tumbling provides less information to the filter regarding the moments.

Overall, the estimated parameters most sensitive to changes in the level of truth tumbling are the spin state angular velocity and the moments of inertia. The spin state orientation, small body GM, and spacecraft errors are also affected, though to a far lesser extent.

In future works, the authors plan to use Modified Rodriguez Parameters with the shadow switching method to represent the spacecraft attitude as it is done for small body spin state, allowing for a three dimensional representation of the attitude that has no risk of singularity issues. The authors also plan to vary the amount of tumbling in the truth spin state as part of a Monte Carlo analysis, versus only three scenarios. This analysis will better assess the limitations of the SLAM algorithm.

Additional future work includes employing a sigma point filter rather than the EKF to better handle the nonlinearities in the dynamics and measurement models. The authors may also attempt to estimate center of mass offset of the small body, though the observability of this offset may be limited for the same reasons that the moments of inertia observability is limited.

Possible modeling improvements include using a polyhedron shape model rather than a triaxial ellipsoid and including camera optical distortion effects. The authors also plan to compare the results from running with other small bodies of different sizes and shapes, and levels of tumbling, allowing a further exploration and refinement of the feasibility of tumbling estimation in various scenarios. Different spacecraft trajectories may also be considered, to determine if certain orbital regimes provide better estimation of the spin state for a tumbling small body.

CONCLUSIONS

In this paper, an EKF SLAM algorithm effectively estimates the small body spin states for several different tumbling small body scenarios, as well as the spacecraft position, velocity, and attitude; small body mass and moments of inertia; and visible landmark surface positions. The estimation converges successfully for large initial state errors, with order of magnitude error decreases in the small body spin state attitude and angular velocity; spacecraft position and velocity; and small body GM. Landmark surface position errors are also reduced by a minimum factor of 3 for these scenarios. Unfortunately the small body moments of inertia have lower levels of observability for these scenarios.

For each of the three different truth tumbling scenarios evaluated, the maximum initial small body attitude error magnitude and initial small body angular velocity error magnitude that the estimation algorithm can handle without significant degradation is evaluated. It is revealed that while the initial orientation error needs to be within 50 degrees 1-sigma (and within 10 degrees 1-sigma for the faster tumbling scenario), the initial angular velocity error can be very large (up to 1500 or 2000 deg/day 1-sigma) and the SLAM estimation will still converge. This is a critical result, as it shows that if the initial angular velocity of the body is completely incorrect, the SLAM estimation algorithm can still converge on the correct values. Thus, upon arrival at a small body that is tumbling, as long as the spacecraft can determine the initial orientation using landmarks within reasonable accuracy, the angular velocity can be estimated with no prior knowledge.

The estimation performance also shows some sensitivity to the accuracy of attitude errors provided by the separate attitude determination system. Additionally it is observed that a small amount of measurement underweighting produces slightly better results. Finally, it is observed that higher levels of tumbling in the small body increase the spin state angular velocity estimation errors and decrease the inertia moments error, as expected.

To the authors knowledge, this is the first application of a SLAM algorithm to estimate the spin state of a tumbling small body. By deploying an EKF SLAM estimation algorithm, many of the relevant quantities for successful navigation of current small body missions are simultaneously estimated. Thus, the estimation technique and tuning parameters used may prove useful to future mission planners and operators of missions to small bodies. And if this tool is placed in an autonomous navigation framework, it has the potential to significantly reduce the ground resources that are currently required to navigate a small body mission, as well as increase the spacecraft autonomous capabilities.

ACKNOWLEDGMENT

The work described in this paper was funded by NASA's Chief Technology Office through a NASA Space Technology Research Fellowship.

REFERENCES

[1] S. Bhaskaran *et al.*, "Rosetta Navigation at Comet Churyumov-Gerasimenko," *38th AAS GN&C Conference*, 2015. AAS 15-122.

[2] P. L. Lamy, I. Toth, B. J. Davidsson, O. Groussin, P. Gutiérrez, L. Jorda, M. Kaasalainen, and S. C. Lowry, "A portrait of the nucleus of comet 67P/Churyumov-Gerasimenko," *Space science reviews*, Vol. 128, No. 1-4, 2007, pp. 23–66.

[3] P. Pravec, A. Harris, D. Vokrouhlickỳ, B. Warner, P. Kušnirák, K. Hornoch, D. Pray, D. Higgins, J. Oey, A. Galád, *et al.*, "Spin rate distribution of small asteroids," *Icarus*, Vol. 197, No. 2, 2008, pp. 497–504.

[4] D. J. Scheeres, *Orbital Motion in Strongly Perturbed Environments*. Springer, 2012.

[5] T. Bailey, J. Nieto, J. Guivant, M. Stevens, and E. Nebot, "Consistency of the EKF-SLAM algorithm," *Intelligent Robots and Systems, 2006 IEEE/RSJ International Conference on*, IEEE, 2006, pp. 3562–3568.

[6] C. Cocaud and T. Kubota, "Autonomous navigation near asteroids based on visual SLAM," *Proceedings of the 23rd International Symposium on Space Flight Dynamics, Pasadena, California*, 2012.

[7] S. Bhaskaran, S. Nandi, S. Broschart, M. Wallace, L. Cangahuala, and C. Olson, "Small Body Landings Using Autonomous Onboard Optical Navigation," *The Journal of the Astronautical Sciences*, Vol. 58, No. 3, 2011, pp. 409–427.

[8] C. Olson, "Analysis of Asteroid Landing Capabilities Using Autonomous Optical Navigation," Master's thesis, The University of Texas at Austin, Austin, TX, 2009.

[9] C. Olson, R. Russell, and J. Carpenter, "Small Body Optical Navigation Using The Additive Divided Difference Sigma Point Filter," *25th AAS/AIAA Space Flight Mechanics Meeting*, 2014. AAS 14-422.

[10] P. K. Seidelmann, B. Archinal, M. Ahearn, A. Conrad, G. Consolmagno, D. Hestroffer, J. Hilton, G. Krasinsky, G. Neumann, J. Oberst, *et al.*, "Report of the IAU/IAG Working Group on cartographic coordinates and rotational elements: 2006," *Celestial Mechanics and Dynamical Astronomy*, Vol. 98, No. 3, 2007, pp. 155–180, 10.1007/s10569-007-9072-y.

[11] C. D. Karlgaard and H. Schaub, "Nonsingular attitude filtering using modified Rodrigues parameters," *The Journal of the Astronautical Sciences*, Vol. 57, No. 4, 2009, pp. 777–791.

[12] D. Scheeres and R. Schweickart, "The mechanics of moving asteroids," *2004 Planetary Defense Conference: Protecting Earth from Asteroids*, 2004, pp. 23–26.

[13] D. Koschny, R. Solaz, and C. Vallat, "Rosetta Project Glossary," Jan 2007. RO-EST-LI-5012, URL: http://www.rssd.esa.int/index.php?project=rosetta&page=glossary#CAM [retrieved 9 September 2014].

[14] C. Russell *et al.*, "Dawn mission to Vesta and Ceres," *Earth, Moon, and Planets*, Vol. 101, No. 1-2, 2007, pp. 65–91, 10.1007/s11038-007-9151-9.

[15] S. Hawkins III, "Overview of the Multi-Spectral Imager on the NEAR spacecraft," *Acta Astronautica*, Vol. 39, No. 1, 1996, pp. 265–271, 10.1016/s0094-5765(96)00144-0.

[16] M. Ishiguro *et al.*, "The Hayabusa Spacecraft Asteroid Multi-band Imaging Camera (AMICA)," *Icarus*, Vol. 207, No. 2, 2010, pp. 714–731, 10.1016/j.icarus.2009.12.035.

[17] N. Mastrodemos, B. P. Rush, and W. Owen, Jr., "Optical Navigation For the Rosetta Mission," *38th AAS GN&C Conference*, 2015. AAS 15-123.

[18] W. Owen, Jr., "Methods of Optical Navigation," *21st AAS/AIAA Space Flight Mechanics Meeting*, New Orleans, LA, 2011. AAS 11-215.

[19] B. Tapley, B. Schutz, and G. Born, *Statistical Orbit Determination*. Elsevier Academic Press, 2004.

[20] A. Landi, F. Boldrini, and D. Procopio, "Mars Express and Rosetta Autonomous Str: in Flight Experience," *Guidance, Navigation and Control Systems*, Vol. 606, 2006, p. 55.

[21] C. Liebe, "Accuracy performance of star trackers-a tutorial," *Aerospace and Electronic Systems, IEEE Transactions on*, Vol. 38, No. 2, 2002, pp. 587–599, 10.1109/taes.2002.1008988.

[22] M. Abrahamson and S. Bhaskaran, "Lidar and Optical-based Autonomous Navigation For Small Body Proximity Operations," *25th AAS/AIAA Space Flight Mechanics Meeting*, Santa Fe, NM, 2014. AAS 14-420.

[23] C. Olson, C. Wright, and A. Long, "Expected Navigation Flight Performance for the Magnetospheric Multiscale (MMS) Mission," *22nd AAS/AIAA Space Flight Mechanics Meeting*, 2012. AAS 12-199.

[24] R. A. Werner, "Spherical harmonic coefficients for the potential of a constant-density polyhedron," *Computers & Geosciences*, Vol. 23, No. 10, 1997, pp. 1071–1077.

[25] R. A. Werner and D. J. Scheeres, "Exterior gravitation of a polyhedron derived and compared with harmonic and mascon gravitation representations of asteroid 4769 Castalia," *Celestial Mechanics and Dynamical Astronomy*, Vol. 65, No. 3, 1996, pp. 313–344.

[26] K.-H. Glassmeier, H. Boehnhardt, D. Koschny, E. Kührt, and I. Richter, "The Rosetta mission: flying towards the origin of the solar system," *Space Science Reviews*, Vol. 128, No. 1-4, 2007, pp. 1–21.

[27] D. Wokes and J. Essert, "Development of Rosetta's Initial Stage Comet Rendezvous Guidance Systems," *AIAA/AAS Astrodynamics Specialist Conference*, 2012.

[28] J. L. Crassidis and F. L. Markley, "Attitude estimation using modified Rodrigues parameters," *Flight Mechanics/Estimation Theory Symposium*, 1996.

[29] T. Bailey and H. Durrant-Whyte, "Simultaneous localization and mapping (SLAM): Part II," *IEEE Robotics & Automation Magazine*, Vol. 13, No. 3, 2006, pp. 108–117.

[30] R. Zanetti, K. DeMars, and R. Bishop, "Underweighting Nonlinear Measurements," *Journal of Guidance, Control, and Dynamics*, Vol. 33, No. 5, 2010, pp. 1670–1675, 10.2514/1.50596.

[31] D. Bayard and P. Brugarolas, "An estimation algorithm for vision-based exploration of small bodies in space," *IEEE American Control Conference*, 2005, pp. 4589–4595, 10.1109/acc.2005.1470719.

[32] C. Gates, "A Simplified Model of Midcourse Maneuver Execution Errors," Tech. Rep. 32-504, Jet Propulsion Laboratory, Pasadena, CA, October 15, 1963.